Seeds of Life in Space (SOLIS). VIII. SiO isotopic fractionation, and a new insight into the shocks of L1157-B1

S. Spezzano, C. Codella, L. Podio, C. Ceccarelli, P. Caselli, R. Neri, A. López-Sepulcre

A&A 640, A74 (2020)
https://doi.org/10.1051/0004-6361/202037864

Astronomy & Astrophysics

Seeds of Life in Space (SOLIS) VIII. SiO isotopic fractionation, and a new insight into the shocks of L1157-B1⋆,⋆⋆

S. Spezzano[1], C. Codella[2,3], L. Podio[2], C. Ceccarelli[3], P. Caselli[1], R. Neri[4], and A. López-Sepulcre[3,4]

[1] Max Planck Institute for Extraterrestrial Physics, Giessenbachstrasse 1, 85748 Garching, Germany
e-mail: spezzano@mpe.mpg.de
[2] INAF, Osservatorio Astrofisico di Arcetri, Largo E. Fermi 5, 50125 Firenze, Italy
[3] Univ. Grenoble Alpes, CNRS, Institut de Planétologie et d'Astrophysique de Grenoble (IPAG), 38000 Grenoble, France
[4] Institut de Radioastronomie Millimétrique, 300 rue de la Piscine, Domaine Universitaire de Grenoble, 38406 Saint-Martin d'Hères, France

Received 2 March 2020 / Accepted 2 June 2020

ABSTRACT

Context. Contrary to what is expected from models of Galactic chemical evolution, the isotopic fractionation of silicon (Si) in the Galaxy has recently been found to be constant. This finding calls for new observations, also at core scales, to re-evaluate the fractionation of Si.
Aims. L1157-B1 is one of the outflow-shocked regions along the blue-shifted outflow that is driven by the Class 0 protostar L1157-mm. It is an ideal laboratory for studying the material ejected from the grains on very short timescales because its chemical composition is representative of the composition of the grains.
Methods. We imaged ^{28}SiO, ^{29}SiO, and ^{30}SiO $J = 2$–1 emission towards L1157-B1 and B0 with the NOrthern Extended Millimeter Array (NOEMA) interferometer as part of the Seeds of Life in Space (SOLIS) large project. We present here a study of the isotopic fractionation of SiO towards L1157-B1. Furthermore, we used the high spectral resolution observations on the main isotopologue, ^{28}SiO, to study the jet impact on the dense gas. We here also present single-dish observations obtained with the IRAM 30 m telescope and *Herschel*-HIFI. We carried out a non-local thermal equilibrium analysis using a large velocity gradient code to model the single-dish observations.
Results. From our observations we can show that (i) the 2–1 transition of the main isotopologue is optically thick in L1157-B1 even at high velocities, and (ii) the [^{29}SiO/^{30}SiO] ratio is constant across the source, and consistent with the solar value of 1.5.
Conclusions. We report the first isotopic fractionation maps of SiO in a shocked region and show the absence of a mass-dependent fractionation in ^{29}Si and ^{30}Si across L1157-B1. A high-velocity bullet in ^{28}SiO has been identified, showing the signature of a jet impacting on the dense gas. With the dataset presented in this paper, both interferometric and single-dish, we were able to study the gas that is shocked at the B1a position and its surrounding gas in great detail.

Key words. ISM: clouds – ISM: molecules – ISM: jets and outflows

1. Introduction

Studying the early stages in stellar and planetary system formation is important for understanding the evolution of matter in the interstellar medium (ISM), and finally our astrochemical origins. In particular, isotopic ratios are of pivotal importance for following the chemical link in the evolution of the material in dense molecular clouds, which are the nursery of new stars, to a planetary system like our own (e.g. Caselli & Ceccarelli 2012, and references therein).

Jets are common in protostars because they are an efficient way to release angular momentum (Frank et al. 2014, and references therein). Jets have a deep effect on the chemical and physical evolution of the ISM. Shocks created by the fast (at least 100 km s^{-1}) jet propagating through the protostellar high-density cocoon are a unique place to study what is released by dust mantles and refractory cores as a consequence of processes such as sputtering and shattering (Bachiller et al. 2001; Fontani et al. 2014; Codella et al. 2017; Lefloch et al. 2017; Cheng et al. 2019; Kong et al. 2019; Ospina-Zamudio et al. 2019; Tychoniec et al. 2019).

One prototypical shock laboratory is the L1157 outflow. The Class 0 low-mass protostar L1157-mm, located at 350 pc (Zucker et al. 2019), is characterised by an episodic precessing jet (Gueth et al. 1996; Podio et al. 2016) that produced several shocked regions. L1157-B1 is a shocked region along the outflow driven by L1157-mm. L1157-B1 is one of the best places to study the material released from dust mantles because it is kinematically very young ($\leqslant 2 \times 10^3$ yr) (Codella et al. 2017). Previous observations of L1157-B1 have shown a very rich chemistry (Bachiller et al. 2001; Arce et al. 2008; Codella et al. 2009, 2015, 2017, 2020; Fontani et al. 2014; Lefloch et al. 2017). Interferometric observations show structure at small scale along the southern outflow lobe of L1157: the three large molecular clumps, called B0, B1, and B2, have been resolved into more subclumps (Benedettini et al. 2007). Some of the subclumps in

⋆ The reduced datacubes and spectra are only available at the CDS via anonymous ftp to cdsarc.u-strasbg.fr (130.79.128.5) or via http://cdsarc.u-strasbg.fr/viz-bin/cat/J/A+A/640/A74
⋆⋆ Based on observations carried out with the IRAM NOEMA interferometer. IRAM is supported by INSU/CNRS (France), MPG (Germany) and IGN (Spain).

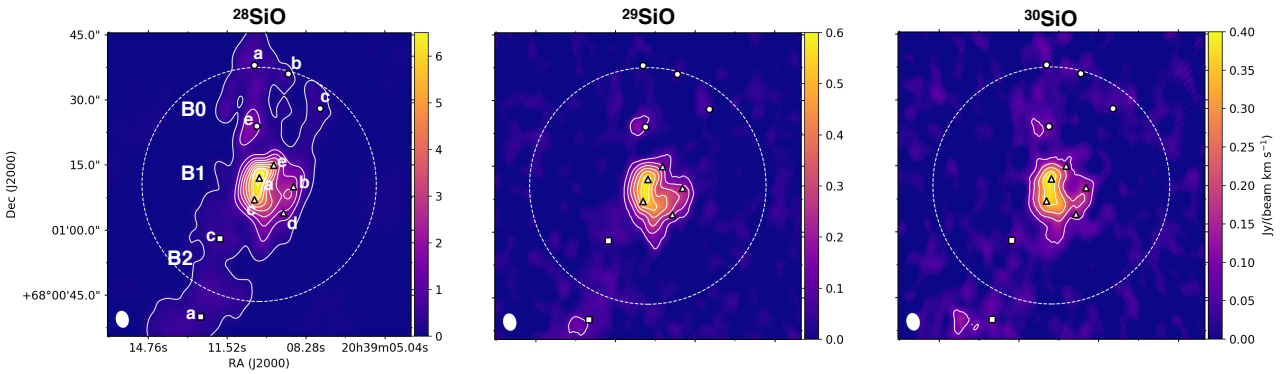

Fig. 1. ^{28}SiO, ^{29}SiO, and ^{30}SiO (2–1) integrated-intensity maps towards L1157-B1, obtained with a velocity resolution of ∼7 km s^{-1} . The emission has been integrated between −22.95 and 6.25 km s^{-1}. The clean beam of 3.8″ × 2.8″ is shown in the bottom left corner of the maps, and the primary beam of 56″ is reported as a dotted white line. The contours for ^{28}SiO start at 5σ (rms = 36 mJy beam^{-1} km s^{-1}), then 30σ, and they then increase with steps of 20σ. The contours for ^{29}SiO start at 5σ (rms = 18 mJy beam^{-1} km s^{-1}), and increase with steps of 5σ. The contours for ^{30}SiO start at 5σ (rms = 17 mJy beam^{-1} km s^{-1}), and increase with steps of 5σ. B0, B1, and B2 are three shock regions along the outflow of L1157. They are composed by several subclumps marked here with circles (B0), triangles (B1), and squares (B2) (Benedettini et al. 2007). The L1157-mm protostar is located towards the north-west at $\Delta\alpha = -25''$and $\Delta\delta = +63.5''$($\alpha_{2000} = 20^h39^m06^s.0$, $\delta_{2000} = +68°02'14''.0$). The maps are not corrected for the primary beam.

B0, B1, and B2 are shown in Fig. 1. Based on the radial velocity of the jet as observed in the inner knots and on the precession model presented in Podio et al. (2016), the kinematical ages of the different shocked regions range from 1340 yr (B0) to 1550 yr (B1a) and 2530 yr (B2) at a distance of 350 pc. In particular, L1157-B1 is a laboratory for studying the molecules that are released in the gas phase from the surface of dust grains and the interplay of the chemistry in the gas phase and in the dust.

SiO is an excellent tracer of shocked gas in outflows. Silicon is released in the gas phase from the grains because of sputtering and grain-grain collisions along the shock, and it is oxidised to SiO (Schilke et al. 1997; Caselli et al. 1997). Therefore, SiO can be studied efficiently in a shock because its abundance is expected to increase by orders of magnitude (Gusdorf et al. 2008a,b; Guillet et al. 2011; Podio et al. 2017, and references therein). The studies of SiO towards L1157-B1 include the interferometric map of the 2–1 transition of the main isotopologue (Gueth et al. 1998), single-dish observations of multiple lines of the main isotopologue (Bachiller & Pérez Gutiérrez 1997; Bachiller et al. 2001; Nisini et al. 2007), and single-dish observations of the rarer isotopologues ^{29}SiO and ^{30}SiO (Podio et al. 2017).

Here we present the first maps of the silicon isotopologues of SiO towards L1157-B1 (^{28}SiO, ^{29}SiO, and ^{30}SiO) observed in the framework of Seeds Of Life In Space (SOLIS; Ceccarelli et al. 2017), an IRAM NOrthern Extended Millimeter Array (NOEMA) large programme aimed at investigating the formation of complex molecules during the early stages of the star formation process. With this dataset we can study the isotopic fractionation of Si around a Sun-like protostar, and better constrain the origin of the SiO high-velocity component. Furthermore, we complement the SOLIS data with previously obtained single-dish observations of SiO emission towards L1157-B1 from $J = 2$–1 to 12–11.

The paper is structured as follows: the observations carried out with NOEMA, the IRAM 30 m telescope, and *Herschel*-HIFI are presented in Sect. 2. The results of the single-dish and interferometric observations are presented in Sect. 3, with a focus on the SiO isotopic fractionation in L1157-B1 and the kinematics. The non-local thermal equilibrium (non-LTE) analysis of the IRAM 30 m spectra is summarised in Sect. 4. In Sect. 5 we discuss the isotopic fractionation of SiO in the framework of the Galactic chemical evolution (GCE), as well as the signature of the jet coming from the protostar L1157-mm. Finally, our conclusions are summarised in Sect. 6.

2. Observations

2.1. NOEMA

L1157-B1 was observed for 6.7 h at 3 mm with the IRAM NOEMA array during one track on April 7, 2018 (nine antennas), using the C configuration. The shortest and longest projected baselines are 24 m and 644 m, respectively. The phase centre is $\alpha_{2000} = 20^h39^m10^s.21$, $\delta_{2000} = +68°01'10''.5$. The ^{28}SiO, ^{29}SiO, and ^{30}SiO $J = 2$–1 lines listed in Table 1 were observed using the Polyfix correlator, with a total spectral band of ∼8 GHz and a spectral resolution of 2.0 MHz (7.3 km s^{-1}). The main isotopologue was also observed at high spectral resolution (62.5 kHz, 0.22 km s^{-1}). Calibration was carried out following standard procedures, using GILDAS-CLIC[1]. The bandpass was calibrated on 3C84, while the absolute flux was fixed by observing LkHα101, 2010 + 723, and 1928 + 738. The final uncertainty on the absolute flux scale is ⩽10%. The phase rms was ⩽60°, the typical precipitable water vapour (pwv) was ∼6–10 mm, and the system temperature ∼80–120 K. Images were produced using natural weighting and were restored with a clean beam of 3.″8 × 2.″8 (PA = −167.8°). The rms noise in the broadband cubes was 0.6-1.7 mJy beam^{-1}, depending on the frequency. Our NOEMA observations recover 80% of the flux from the ^{28}SiO (2–1) emission compared to the IRAM 30 m observations; see Appendix B. The integrated intensities of the rarer isotopologues in both the NOEMA and IRAM 30 m spectra match within 20%. This is consistent with the calibration error of the observations and therefore does not affect the quantities that we derive in the isotopic ratio maps.

2.2. IRAM 30 m

The single-dish observations of the SiO, ^{29}SiO, and ^{30}SiO lines from $J = 2$–1 to $J = 8$–7 (see Table 1 for the frequencies) were obtained using the IRAM 30 m antenna in the context of the Astrochemical Surveys At IRAM large programme (ASAI;

[1] http://www.iram.fr/IRAMFR/GILDAS/

Table 1. Properties of the detected transitions from SiO, ^{29}SiO, and ^{30}SiO in L1157-B1 (single-dish ASAI+CHESS spectra).

Line	Frequency [a] MHz	E_{up} (K)	*HPBW* (″)	rms (mK)	V_{peak} (km s^{-1})	$T_{mb-peak}$ (K)	$\int T_{mb} dV$ [−23, −13] (K km s^{-1})	[−13, −3] (K km s^{-1})	[−3, +5] (K km s^{-1})
					SiO				
2–1	86 846.96	6	28	2	−1.6	1.72	1.51 ± 0.01	8.22 ± 0.01	9.60 ± 0.01
3–2	130 268.61	13	19	9	−0.2 [b]	2.86	1.93 ± 0.03	12.13 ± 0.03	17.41 ± 0.03
5–4	217 104.98	31	11	3	−1.6	2.51	2.58 ± 0.01	13.03 ± 0.01	15.11 ± 0.01
6–5	260 518.02	44	9	5	−1.6	1.69	1.66 ± 0.02	8.93 ± 0.02	9.37 ± 0.02
8–7	347 330.59	75	7	17	−1.6	0.93	0.83 ± 0.06	5.75 ± 0.06	4.49 ± 0.06
12–11 [c]	520 881.09	163	41	13	−1.6	0.04	<0.05	0.17 ± 0.05	0.06 ± 0.04
					^{29}SiO				
2–1	85 759.20	6	29	1	−1.6	0.19	0.12 ± 0.01	0.74 ± 0.01	– [c]
3–2	128 637.05	12	19	10	−1.6	0.24	0.18 ± 0.04	1.03 ± 0.04	1.34 ± 0.03
5–4	214 385.75	31	11	3	−1.6	0.16	0.11 ± 0.01	0.72 ± 0.01	0.83 ± 0.01
6-5	257 255.22	43	10	4	−1.6	0.11	0.07 ± 0.02	0.46 ± 0.02	0.49 ± 0.01
7–6	300 120.47	58	8	10	−1.6	0.05	<0.04	0.25 ± 0.04	0.18 ± 0.03
8–7	342 980.84	74	7	25	–	–	<0.1	<0.1	<0.1
12–11 [c]	514 359.34	161	41	13	–	–	<0.05	<0.05	<0.05
					^{30}SiO				
2–1	84 746.17	6	29	1	−1.6	0.10	0.10 ± 0.01	0.49 ± 0.01	0.52 ± 0.01
4–3	169 486.88	20	15	28	−1.6	0.17	<0.1	0.6 ± 0.1	0.7 ± 0.1
5–4	211 853.47	31	12	3	−1.6	0.11	0.06 ± 0.01	0.53 ± 0.01	0.57 ± 0.01
6–5	254 216.66	43	10	3	−1.6	0.08	0.07 ± 0.01	0.35 ± 0.01	0.39 ± 0.01
12–11 [d]	508 285.78	159	42	12	–	–	<0.05	<0.05	<0.05

Notes. [a]Müller et al. (2013). [b]The velocity difference between the 3–2 ^{28}SiO transition and all other transitions reported here is only one velocity channel, hence we consider its velocity in accordance with the others. [c]The integrated intensity at low velocities of the 2−1 transition of ^{29}SiO is not reported here because the line is blended with the $4_{1,3}$–$3_{-2,2}$ transition of $^{13}CH_3OH$. [d]The 12−11 transitions are taken with *Herschel*-HIFI (LP CHESS). All the other spectra are taken with the IRAM 30 m (LP ASAI).

Lefloch et al. 2018). The spectra are shown in Fig. 2. Observations were made in wobbler mode at the position of the B1 shock, that is, at $\alpha_{2000} = 20^h\ 39^m\ 10\overset{s}{.}2$, $\delta_{2000} = +68°\ 01'\ 10\overset{''}{.}5$, or in other words, at $\Delta = +25''$ and $\Delta = -63\overset{''}{.}5$ from the L1157-mm protostar. Our observations were performed during several runs in 2011 and 2012 using the EMIR receiver connected with the FTS spectrometers. This provided a spectral resolution of 200 kHz (i.e. 0.2–0.7 km s^{-1}, depending on the frequency). More details can be found in Lefloch et al. (2018). The weaker spectra were smoothed to 1.4 km s^{-1} to increase the signal-to-noise ratio (S/N). The half-power beam width (HPBW) spans from 7″ to 29″, depending on the frequencies. The forward (F_{eff}) and beam (B_{eff}) efficiencies are in the 0.80-0.95 and 0.34-0-81 ranges, respectively. The final rms, in main-beam temperature, extends from 1 (at 85 GHz) to 25 mK (342 GHz).

2.3. Herschel-HIFI

The SiO, ^{29}SiO, and ^{30}SiO $J = 12$–11 transitions (Table 1 reports their frequencies) were observed with *Herschel*-HIFI on October 27, 2010, and August 1, 2009 during the unbiased spectral survey CHESS (e.g. Ceccarelli et al. 2010) with the HIFI bands 1a at the same position as was used for the IRAM 30 m observations. The spectra are shown in Fig. 2. A receiver in double side-band mode was used, with a total integration time of 8912 s. The Wide Band Spectrometer was used, with a velocity resolution of about 0.15 km s^{-1}. The SiO(12–11) spectrum was successively smoothed to 4 km s^{-1} to increase the S/N. The forward (F_{eff}) and beam (B_{eff}) efficiencies are 0.96 and 0.73, respectively. The HPBW is about 42″ (Roelfsema et al. 2012). Data were processed with the ESA-supported package HIPE (*Herschel* Interactive Processing Environment) and were analysed using the GILDAS-CLASS software[1]. The flux uncertainty is around 15%. The rms, in main-beam temperature, is about 12–13 mK.

3. Results

3.1. Single-dish spectra

We detected six lines of ^{28}SiO (up to $J = 12$–11), five lines of ^{29}SiO (up to $J = 7$–6), and four lines of ^{30}SiO (up to $J = 6$–5). Together, they form a large SiO dataset (spanning from 86 to 521 GHz). The spectra are shown in Fig. 2 and the line properties are summarised in Table 1. The SiO lines peak at a blue-shifted velocity, approximately −4 km s^{-1} with respect to the systemic velocity ($v_{sys} = +2.6$ km s^{-1}). Moreover, the SiO lines show a high-velocity wing that extends up to −20 km s^{-1} and likely originates in the strong shock that occurs where the jet impacts the cavity walls (see Sect. 3.5). The single-dish spectra are used to characterise the physical properties of the emitting gas in the large velocity gradient (LVG) analysis described in Sect. 4. The integrated intensities reported in Table 1 are therefore divided into three velocity intervals: low velocity (LV) from −3 to +5 km s^{-1}, high velocity (HV) from −13 to −3 km s^{-1}, and extremely high velocity (EHV) from −23 to −13 km s^{-1}.

3.2. Integrated-intensity maps

Figure 1 shows the image of the emission of the $J = 2$–1 transitions of ^{28}SiO, ^{29}SiO, and ^{30}SiO obtained with ∼7 km s^{-1} spectral resolution. The intensity was integrated between −22.95

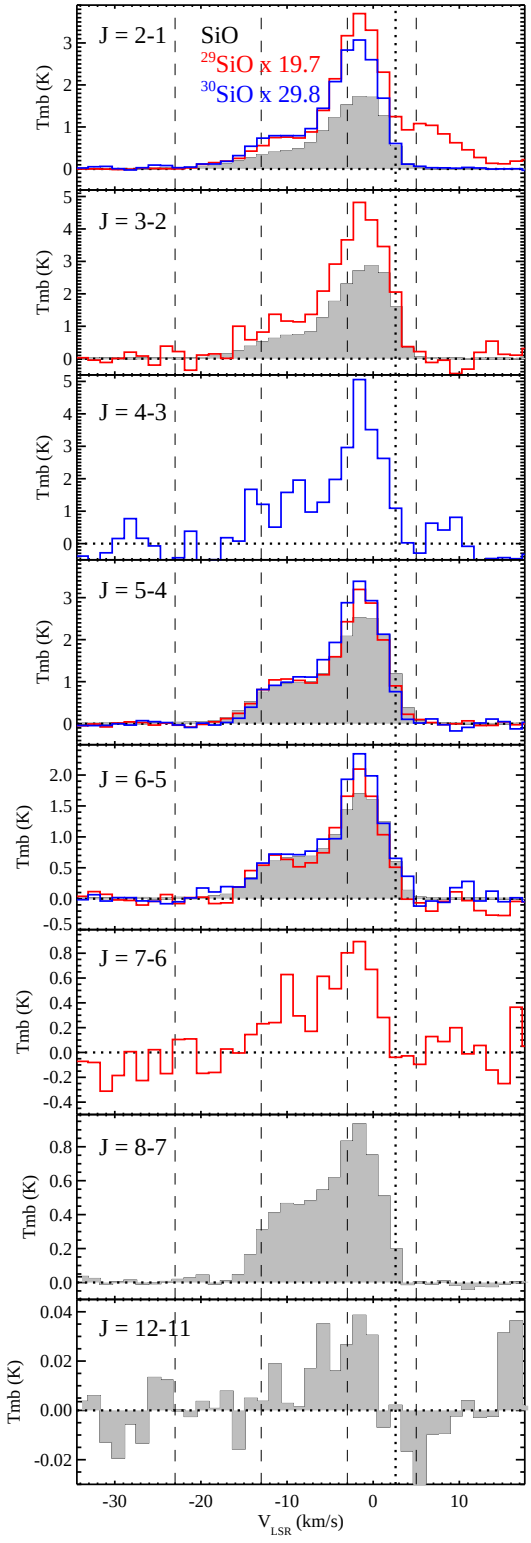

Fig. 2. Line profiles of SiO in the L1157-B1 shock. The line intensity in main-beam temperature ($T_{\rm mb}$) from ^{29}SiO (red), and ^{30}SiO (blue) is over-plotted on the main isotopologue, ^{28}SiO (grey), by multiplying for their solar isotopic ratios ($[^{28}Si/^{29}Si]_\odot = 19.7$, $[^{28}Si/^{30}Si]_\odot = 29.8$, Anders & Grevesse 1989). The transitions are labelled. The baseline and the systemic velocity (+2.6 km s^{-1}, Bachiller et al. 2001) are indicated by the horizontal and vertical dotted lines, respectively. The vertical dashed lines indicate the three velocity intervals where the integrated intensity has been calculated: [−23, −13], [−13, −3], and [−3, +5] km s^{-1}, see Table 1. The red-shifted component that appears to be associated with ^{29}SiO 2−1 is due to blending with the $^{13}CH_3OH$ $4_{1,3}$–$3_{-2,2}$ line.

and 6.25 km s^{-1}, that is, in four channels centred at 2.6, −4.7, −12, and −19.3 km s^{-1}, where emission from the rarer SiO isotopologues is detected (see Sect. 3.3). The channel maps for all three isotopologues are presented in Appendix A (Figs. A.1–A.3). The map of ^{28}SiO (2–1) has previously been reported in Gueth et al. (1998) using the IRAM-PdBI with four antennas. Our NOEMA dataset has an improvement in the noise level of a factor of 20 (rms = 18.3 mJy beam^{-1} vs. 0.9 mJy beam^{-1}) and allows us to image higher (blue) velocities, up to –20 km s^{-1}, as described in more detail in Sect. 3.4. The integrated-intensity maps in Fig. 1 show the structure of the bow shock B1, the B0 wall, and also some structure towards the shocked region B2. The rarer isotopologues show the same emission morphology as the main isotopologue, ^{28}SiO, with the maximum located at $\alpha_{2000} = 20^{\rm h}39^{\rm m}10^{\rm s}.26$, $\delta_{2000} = +68°01'10''.61$. This position is consistent within the beam size with the B1a clump shown in Benedettini et al. (2007). It is thought to be the position where the precessing jet driven by L1157-mm impacts the cavity wall (Gueth et al. 1998). The rarer isotopologues also trace the so-called "finger" in the south part of B1, which is identified at low velocities in SiO (Gueth et al. 1998) and in CS (Benedettini et al. 2007). This finger lies along the jet direction and is thought to be associated with the magnetic precursor of the shock (Bachiller et al. 2001). Because B2 is outside the primary beam, we are cautious of quantitative measurements towards that position.

3.3. SiO isotopic fractionation in L1157-B1

While the emission of the main isotopologue, ^{28}SiO, is detected with more than 5σ in all six channels shown in Fig. A.1, the rarer isotopologues are detected only in the central four channels, from +2.6 to –19.3 km s^{-1}, shown in Figs. A.1 and A.3. For this reason, we only used these channels to compute the integrated intensity maps (Fig. 1) and the isotopic ratio maps (Fig. 3). A threshold of 5σ was applied to the maps of the different isotopologues before we computed the isotopic ratio maps. The solar isotopic ratios are $[^{28}Si/^{29}Si] = 19.7$, $[^{28}Si/^{30}Si] = 29.8$, and $[^{29}Si/^{30}Si] = 1.5$ (Anders & Grevesse 1989).

The $[^{28}SiO/^{29}SiO]$ and $[^{28}SiO/^{30}SiO]$ ratios in the maps shown in Fig. 3 (upper and middle panel) are lower than the solar ratios (shown as a dotted box in the colour bar), which can be interpreted as indirect proof that the ^{28}SiO (2–1) line is optically thick in the whole region and at all velocities that we imaged. Podio et al. (2017) measured the $[^{28}SiO/^{29}SiO]$ and $[^{28}SiO/^{30}SiO]$ ratios from single-dish observations of the (5–4) and (6–5) transitions, and showed that while the high-velocity wings are in agreement with the solar isotopic ratios, in the low velocities, the ratios are 10–15% lower, suggesting a high optical depth of the main isotopologue.

In contrast to what happens in the isotopic ratio maps for the main isotopologue, the $[^{29}SiO/^{30}SiO]$ ratio shown in the lower panel of Fig. 3 is quite uniform around the solar ratio of 1.5 in all channels except for the channel at +2.6 km s^{-1}. This deviation can be explained with a contamination by the $4_{1,3}$–$3_{-2,2}$ transition of $^{13}CH_3OH$, as shown in Fig. 2 of Podio et al. (2017). The value of the $[^{29}SiO/^{30}SiO]$ ratio averaged within a beam in the channel at –19.3 km s^{-1} is 1.14, while in the channels at –12.0 and –4.7 km s^{-1} , it ranges from 1.1 to 1.5. With an uncertainty of ∼20% in our maps and of ∼5% in the solar isotopic ratio (Anders & Grevesse 1989), these values are consistent with the solar value of 1.5 and do not show any variation across the source. Studying the isotopic fractionation in Galactic sources (as L1157-B1) and comparing it with the solar value (defined 4.6 Gyr ago) gives information on the environment in which

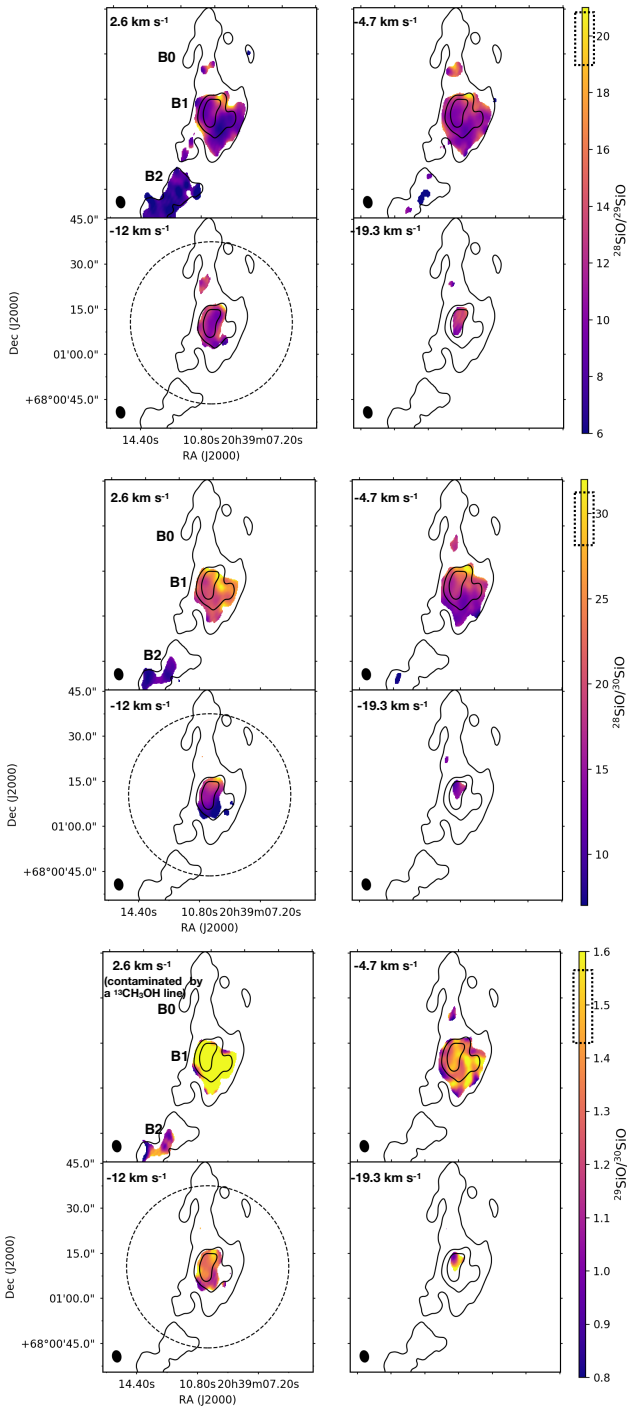

Fig. 3. *Top*: ^{28}SiO/^{29}SiO, *middle*: ^{28}SiO/^{30}SiO, and *bottom*: ^{29}SiO/^{30}SiO isotopic ratio channel maps. The clean beam of 3.8″ × 2.8″ is shown in the bottom left corner of the maps, and the primary beam of 56″ is reported as a dotted black circle. The contours show the 10, 60, and 120σ levels of the integrated intensity map of ^{28}SiO, shown in Fig. 1. The solar isotopic ratio of [^{28}Si/^{29}Si] = 19.7, [^{28}Si/^{30}Si] = 29.8, and [^{29}Si/^{30}Si] = 1.5, including a 5% error, is reported as a dotted box in the colour bar (Anders & Grevesse 1989).

the Sun and solar system were formed, and also on the processes that formed them. Our results confirm what was reported in Podio et al. (2017) based on single-dish observations: the Si isotopic ratios did not change significantly in the past 4.6 billion years. Furthermore, based on our dataset, we can now exclude

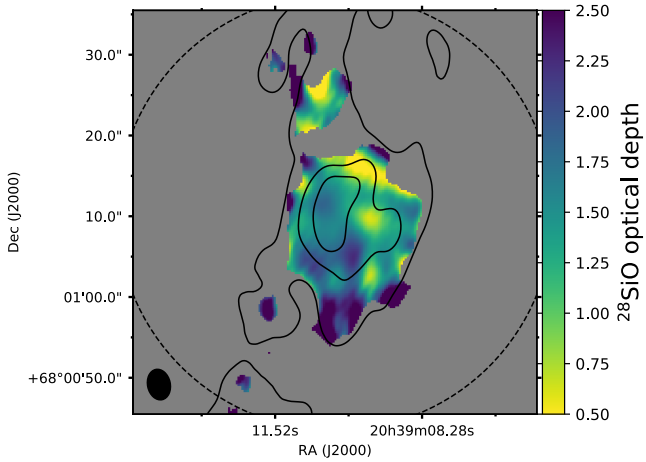

Fig. 4. ^{28}SiO (2–1) optical depth map computed from the ^{28}SiO/^{30}SiO ratio assuming the solar isotopic ratio [^{28}Si/^{30}Si] = 29.8. The contours show the 10, 60, and 120σ levels of the integrated intensity map of the ^{28}SiO, shown in Fig. 1. The primary beam of 56″ is reported as a dotted black circle.

local changes in the isotopic ratios within the shocked region in L1157-B1.

We computed the optical depth (τ) map for the ^{28}SiO (2–1) transition across the core, see Fig. 4. Following Mangum & Shirley (2015), we computed the optical depth of the main isotopologue assuming that the emission of both ^{28}SiO and ^{30}SiO is co-spatial, that the atomic solar ratio of [^{28}Si/^{30}Si] = 29.8 is the same as the molecular ratio, and that the two isotopologues have similar line profiles:

$$\frac{\int T_{\rm R}(^{28}{\rm SiO}){\rm d}V}{\int T_{\rm R}(^{30}{\rm SiO}){\rm d}V} = \frac{1-\exp^{-\tau(^{28}{\rm SiO})}}{1-\exp^{-29.8\tau(^{28}{\rm SiO})}}. \quad (1)$$

Towards the B0 and B1 clumps, the values of τ averaged within a beam range from 1.0 to 2.2, which is similar to the values reported in Podio et al. (2017), which were derived from single-dish observations (τ = 0.7–1.9). The southern clump B2 is outside the primary beam and hence not considered in this discussion.

3.4. Kinematics: the jet signature

As reported in Sect. 2, we also imaged the main isotopologue, ^{28}SiO, with high-velocity resolution (0.22 km s^{-1}). We successively smoothed the spectra to 0.5 km s^{-1} in order to further increase the S/N (see Fig. 5 for a sample of spectra), and obtained an unprecedented view of the high-velocity component of the (2–1) transition. This allowed us to search for signatures of the expected impacts of the jet against the cavity walls. In Fig. 5, we show three representative velocity channel maps, at very high (−19.72 km s^{-1}), high (−10.70 km s^{-1}), and low velocity (−1.22 km s^{-1}). Using these images, we selected the intensity peaks and extracted the corresponding spectra (see Fig. 5, bottom left panel). As a first result, we confirm that the highest velocity SiO emission (see the channel map centred at −10.70 km s^{-1}) within the B1 structure is associated with the B1a clump (Benedettini et al. 2007). This position is indeed considered the youngest impact between the jet (which has never been directly imaged outside the protostar; Podio et al. 2016) and the B1 cavity (see also Busquet et al. 2014 and Benedettini et al. 2012 on H_2O, OI, and high-J CO PACS *Herschel* data).

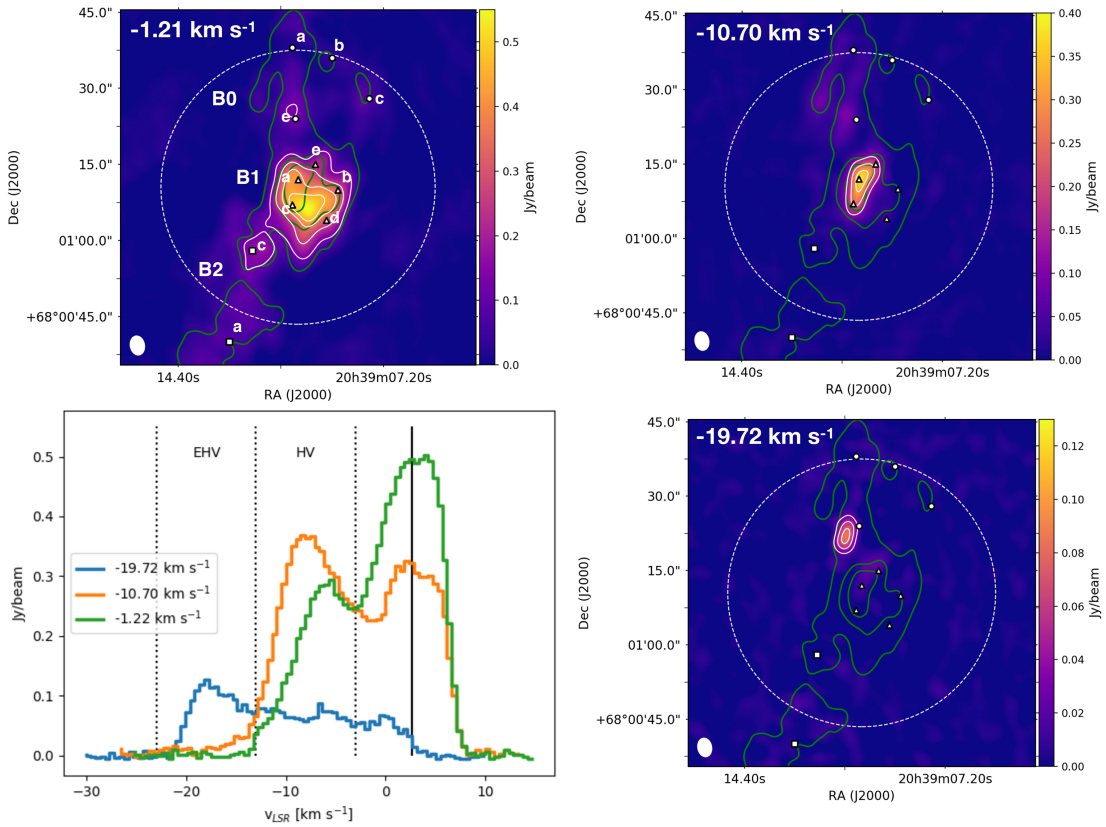

Fig. 5. Velocity channel maps of ^{28}SiO observed with high spectral resolution (0.5 km s^{-1}) at very high (−19.72 km s^{-1}), high (−10.70 km s^{-1}), and low velocity (−1.22 km s^{-1}), and the spectra (*bottom left*) extracted at the position of the intensity peak in each channel. The white contours in the −19.72 km s^{-1} channel map start at 5σ, with steps of 5σ (rms = 5 mJy beam^{-1}). The white contours in the −10.70 km s^{-1} channel map start at 25σ, with steps of 20σ. The white contours in the −1.22 km s^{-1} channel map start at 25σ, with steps of 25σ. The clean beam of 3.8″ × 2.8″ is shown in the bottom left corner of the maps, and the primary beam of 56″ is reported as a dashed white circle. The green contours in the channel maps show the 10, 60, and 120σ levels of the integrated intensity map of the ^{28}SiO, shown in Fig. 1. B0, B1, and B2 are three shock regions along the outflow of L1157, and they are composed of several subclumps marked here with circles (B0), triangles (B1), and squares (B2) (Benedettini et al. 2007). The vertical solid line in the spectra shows the systemic velocity of L1157-B1, +2.6 km s^{-1}. The vertical dotted lines show the intervals of velocity used to run the LVG, (−23, −13) km s^{-1} for the EHV and (−13, −3) km s^{-1} for the HV.

Furthermore, our dataset for the first time allows us to image very high velocity SiO emission outside B1, that is, towards the northern B0 clump (see the channel map centred at −19.72 km s^{-1} in Fig. 5). The comparison of the spectra extracted in the three different intensity peaks clearly shows that the low-velocity emission decreases in the B1a and B0 peaks. The green spectrum in Fig. 5 shows a peak close to the systemic velocity of the source (+2.6 km s^{-1}, shown as a vertical line) and a very broad blue-shifted wing, with an indication of a second peak around –7.5 km s^{-1}. The orange spectrum shows a double-peak structure whose blue-shifted peak is brighter than the peak close to the systemic velocity. The extreme is represented by the blue spectrum, which is extracted at the peak position of the –19.72 km s^{-1} channel map. It clearly differs from the other two spectra, showing almost no emission at the systemic velocity and the expected profile for a shock driven by a high-speed jet (see e.g. Lefloch et al. 2015, and references therein). Because B0 is the youngest shock in the region, it provides a unique opportunity for studying which grain species are released by the shock to the gas phase.

3.5. High and extremely high velocity SiO emission maps

In order to better characterise the origin and nature of the SiO-emitting gas, we roughly divided the integrated emission into three intervals based on the spectra shown in Fig. 5 and discussed in the previous section: low velocity (LV) from −3 to +5 km s^{-1}, high velocity (HV) from −13 to −3 km s^{-1}, and extremely high velocity (EHV) from −23 to −13 km s^{-1}.

Figure 6 shows the emission maps of the HV and EHV gas, integrated in the corresponding velocity intervals, and Table 1 reports the integrated intensities in these velocity intervals for all the SiO lines detected with single-dish telescopes. The single-dish spectra are taken within the area marked by the circles in Fig. 6.

The HV emission peaks at the B1a position and is intense over a roundish clump more than 15″ in size. However, the HV emission is not limited to the B1a clump, but also originates from the entire more extended B1 region, as well as from the B0 shock and walls. On the other hand, the EHV emission is more concentrated and presents two distinct peaks at the B1a and B0e positions of similar intensity and spatial extent, about 15″ × 6″. A faint but clearly detected EHV emission is also present along the north wall of B0. This might identify the gas entrained by the jet that impacts B0 and is responsible for the SiO-emission-shocked gas clump in that position (discussed in Sect. 3.4). In the next section, we analyse the gas properties (temperature and density) of the HV and EHV gas.

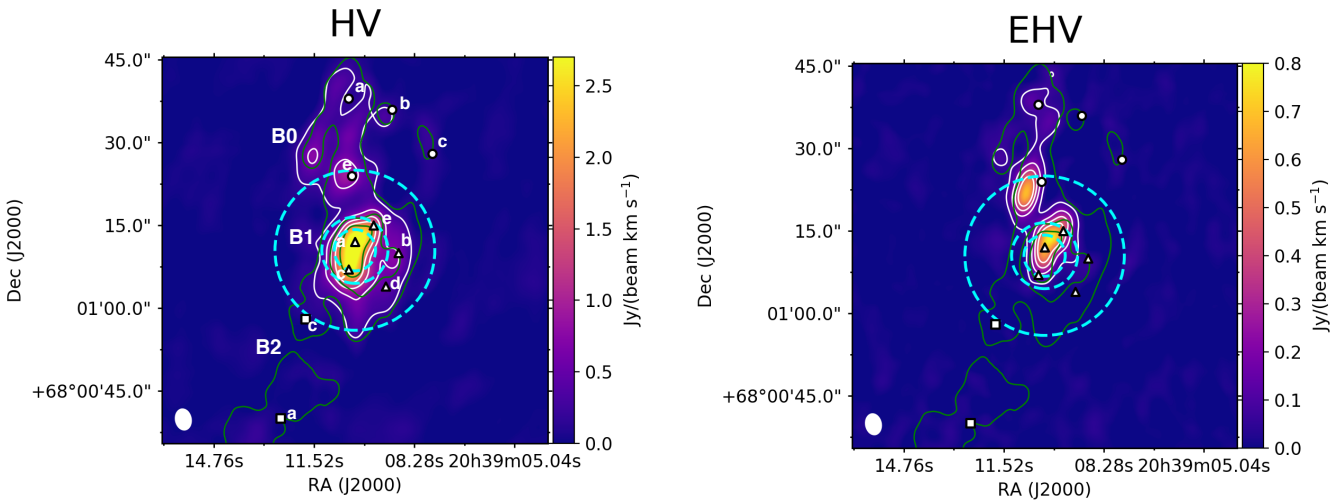

Fig. 6. ^{28}SiO emission integrated over two velocity ranges (see text). EHV: –23 to –13 km s^{-1}, and HV: –13 to –3 km s^{-1}. The white contours start at 5σ, with steps of 15σ (rms = 14 and 45 mJy beam^{-1} for the EHV and HV, respectively). The subclumps composing the B0 and B1 shock regions along the outflow of L1157 are marked here with circles (B0), triangles (B1), and squares (B2). The dashed circles represent the HPBW of the IRAM 30 m spectra at 86 GHz (29″), 210 GHz (12″), and 350 GHz (7.5″). The green contours in the channel maps show the 10, 60, and 120σ levels of the integrated intensity map of ^{28}SiO, shown in Fig. 1.

4. LVG analysis

In this section we analyse the single-dish spectra of the SiO and its isotopologues ^{29}SiO and ^{30}SiO from the 2–1 up to the 8–7 transition (E_{up} from 6 to 163 K), shown in Fig. 2. The 12–11 spectrum was excluded from the analysis because it is too noisy: we note, however, that the fluxes reported in Table 1 are consistent with the solutions provided below. The line properties are summarised in Table 1. This table also reports the integrated intensity in three velocity ranges: EHV: –23 to –13 km s^{-1}, HV: –13 to –3 km s^{-1}, and LV: –3 to +5 km s^{-1}.

In order to derive the average physical properties of the gas that emits SiO, we carried out a non-LTE analysis using the large velocity gradient (LVG) code described in Ceccarelli et al. (2003). We used the collisional coefficients of SiO with H_2 computed between 10 and 300 K for the first 20 levels by Dayou & Balança (2006) that are provided by the BASECOL database (Dubernet et al. 2013).

We ran a large grid of models (≥7000) covering a SiO column density N_{SiO} from 1.5×10^{13} to 8×10^{15} cm^{-2}, a H_2 density n_{H2} from 1×10^{3} to 2×10^{7} cm^{-3}, and a temperature T from 30 to 300 K. We then determined the solution by simultaneously fitting the ^{28}SiO, ^{29}SiO, and ^{30}SiO lines and left as free parameters N_{SiO}, n_{H2} , and T, while the emitting sizes and line widths were those measured. We assumed ^{28}Si/^{29}Si = 19.7 and ^{28}Si/^{30}Si = 29.8, as obtained by Anders & Grevesse (1989) and confirmed by our SOLIS observations for L1157-B1 (see Sect. 3.3), and we added the 20% calibration uncertainty in the observed intensity error bars. We sampled the parameter space unevenly (with steps of 10 K until 100 and 20 K for higher temperatures, steps of a factor of 2 for densities lower than 6×10^{6} cm^{-3} and 1.3 at higher ones, steps of a factor of 1.5 in column densities until 1×10^{14} cm^{-2} and 1.1–1.2 at higher ones to ensure better cover close to the minimum χ^2. The beam dilution was taken into account, assuming that the emitting gas has a circular Gaussian shape and using the standard equation for beam dilution.

We carried out the non-LTE analysis for the HV and EHV components. The results are described in the two following subsections and are summarised in Table 2.

Table 2. Result of the non-LTE LVG analysis.

Component	N_{SiO} $\times10^{12}$ cm^{-2}	Size ″	T K	n_{H2} $\times10^{5}$ cm^{-3}	X_{SiO} $^{(a)}$ $\times10^{-7}$
HV-B1a	40(8)	10(2)	180(36)	6(1)	5(1)
HV-cold	40(8)	25(5)	40(8)	2.0(4)	0.5(1)
EHV-B1a	8(2)	9(2)	180(36)	6(1)	5(1)
EHV-cold	8(2)	20(4)	30(6)	2.0(4)	0.5(1)

Notes. The HV and EHV emissions are composed of two physical components each: the first is associated with the B1a clump, and the second is more extended (see text). $^{(a)}$SiO abundance with respect to molecular hydrogen. The H_2 column density used to calculate the SiO abundance is derived from the CO column density in the g1 and g2 components of the gas in L1157-B1 described in Lefloch et al. (2012), see Sect. 5.3. Numbers in parentheses are one standard deviation in units of the least significant digit. The errors on the sizes are derived from the observations.

4.1. High-velocity component

As shown in Fig. 6 and discussed in Sect. 3.5, the HV SiO emission extends over a size of 15″ centred on B1a, with a halo encompassing the whole B1 region and the B0 wall. We therefore started our non-LTE analysis considering that the emission originates in the roundish 15″ B1a clump, but were unable to find a good enough fit for all the J = 2–1 to 8–7 ^{28}SiO, ^{29}SiO, and ^{30}SiO lines. When shocked regions such as L1157-B1 are observed, several gas components in the line of sight have to be taken into consideration, as described by Lefloch et al. (2012). We then proceeded with a model with two physical components, as suggested in the HV emission map by the presence of the B1 and part of the B0 regions, see Fig. 6. To constrain the parameters of the gas around B1a, we used the three lines with a beam size approximately covering the B1a clump, that is, those with J from 5–4 to 8–7.

The comparison between the observed and the theoretical integrated intensities provides a very good solution, with well-constrained parameters: N_{SiO} = 3–8 $\times10^{13}$ cm^{-2} for an emitting

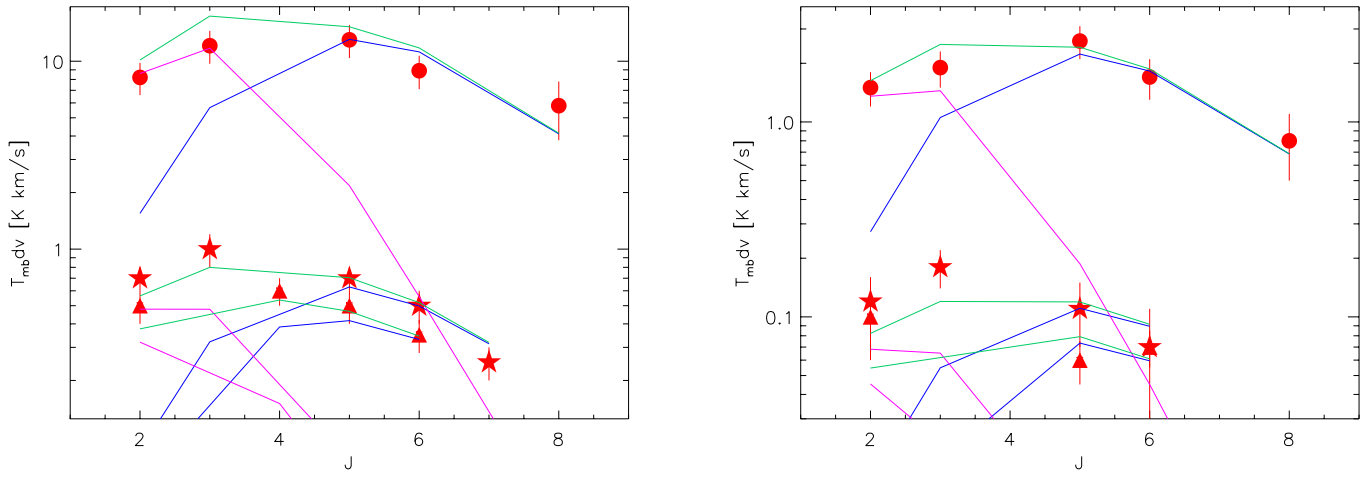

Fig. 7. Result of the simultaneous fit of the ^{28}SiO (circles), ^{29}SiO (stars), and ^{30}SiO (triangles) fluxes of the HV (*left panel*) and EHV (*right panel*) components (Table 1) as a function of the upper level J of the transition. The HV best fit is obtained with two components: (i) a cold component (magenta curves) with $T = 40$ K, $n_{H2} = 2 \times 10^5$ cm^{-3}, and $N_{SiO} = 4 \times 10^{13}$ cm^{-2} that extends 25″, and (ii) a warm component associated with B1a (blue curves) with $T = 180$ K, $n_{H2} = 6 \times 10^5$ cm^{-3}, $N_{SiO} = 4 \times 10^{13}$ cm^{-2} and sizes = 10″. The sum of the two components (green curves) fits the observations very well. Similarly, the EHV best fit is obtained with two components: (i) a cold component (magenta curves) with $T = 30$ K, $n_{H2} = 2 \times 10^5$ cm^{-3}, and $N_{SiO} = 8 \times 10^{12}$ cm^{-2}, that extends 20″, and (ii) a warm component associated with B1a (blue curves) with $T = 180$ K, $n_{H2} = 6 \times 10^5$ cm^{-3} and $N_{SiO} = 8 \times 10^{12}$ cm^{-2} that extends 9″. The sum of the two components (green curves) fits the observations very well.

size 10″ (i.e. approximately the observed full width at half-maximum of the HV emitting gas around B1a, shown in Fig. 6), n_{H2} between 10 and 4 $\times 10^5$ cm^{-3} and T between 90 and 250 K, with the best-fit n_{H2}–T lying along a degenerate but very well constrained curve, where higher densities correspond to lower temperatures. We then searched for a fit with two physical components, the first from the previous fit of the $J = 5$–4 to 8–7 lines, and the second found by best fitting the residuals of all lines. We obtain a final very good fit (reduced $\chi^2 = 1.14$ with 11 degrees of freedom) with (i) a warm component associated with the B1a clump with $T \sim 180$ K, $n_{H2} \sim 6 \times 10^5$ cm^{-3}, and $N_{SiO} \sim 4 \times 10^{13}$ cm^{-2}; (ii) a colder component with $T \sim 40$ K, $n_{H2} \sim 2 \times 10^5$ cm^{-3} and $N_{SiO} \sim 4 \times 10^{13}$ cm^{-2} whose extent is about 40″ × 15″. The theoretical and observed fluxes are shown in Fig. 7. A similarly good fit is also obtained considering for the warm B1a component $T = 100$ K and $n_{H2} = 1 \times 10^6$ cm^{-3} ($\chi^2 = 1.45$) or $T = 250$ K and $n_{H2} = 4 \times 10^6$ cm^{-3} ($\chi^2 = 1.16$).

4.2. Extremely high velocity component

The SiO $J = 2$–1 map of Fig. 6 shows that the EHV emission is split into two clumps about 15″ × 6″, centred on B1a and B0. We started with a single-component fit with an emitting size equal to 18″, approximately the sum of the two clumps in the EHV map. We obtained a relatively good solution ($\chi^2 = 1.8$ for nine degrees of freedom) with $N_{SiO} = 8 \times 10^{12}$ cm^{-2}, n_{H2} between 1 and 7×10^5 cm^{-3}, and T between 80 and 300 K, with the best fit n_{H2}–T lying along a degenerate but very well constrained curve, where higher densities correspond to lower temperatures.

However, there is no reason to assume that the gas temperature and density are the same in the two clumps, therefore we also considered a fit with lines that encompassed the B1a clump alone to have a more constrained view of the parameters in B1a. The best fit of the $J = 5$–4 to 8–7 ^{28}SiO, ^{29}SiO, and ^{30}SiO lines is obtained with $N_{SiO} = 8 \times 10^{12}$ cm^{-2}, $n_{H2} = 6 \times 10^5$ cm^{-3} , and $T = 180$ K; within 1 σ, we obtain N_{SiO} = 4–40 $\times 10^{12}$ cm^{-2}, n_{H2} between 3 and 10 $\times 10^5$ cm^{-3}, and T between 120 and 300 K, always along a degenerate curve as above. We then proceeded, as for the HV case, to fit the residuals to constrain the parameters of a second physical component probed by the EHV emission. However, because the three lines ($J = 5$ to 8) do not cover the B0 region, we only used the $J = 2$–1 and 3–2 to constrain the EHV component in B0. With this caveat, we obtained a best fit of the second component with $N_{SiO} \sim 8 \times 10^{12}$ cm^{-2}, $n_{H2} \sim 2 \times 10^5$ cm^{-3}, and $T \sim 30$ K whose extent is about 30″ × 15″, indicating that the $J = 2$–1 and 3–2 line emission is still dominated by the large scale encompassed by the single-dish measurements rather than the B0 clump. The obtained solution is shown in Fig. 7.

5. Discussion

5.1. Isotopic fractionation and Galactic chemical evolution

Isotopic fractionation is a key observable for understanding the chemical evolution of the Universe. When the evolution of our Solar System is studied by observing the isotopic fractionation in some key elements, we are able to distinguish among solar and pre-solar material, and hence derive information about the physical conditions of the pre-solar nebula, just before the formation of the Solar System (e.g. Hoppe et al. 2018). Moreover, isotopic fractionation can be used to obtain insights inot star formation and evolution (Timmes & Clayton 1996). Monson et al. (2017) showed that secondary (^{29}Si and ^{30}Si) to primary (^{28}Si) isotope ratios of silicon do not show any detectable variation along the Galactic radius. This is an interesting result because of the large (≥900%) variations observed in the secondary-to-primary oxygen isotope ratios. It is also interesting because GCE predicts that the silicon and oxygen isotopic ratios evolve in parallel with a nearly constant ratio in the secondary isotopes (^{29}Si/^{30}Si), and an increasing secondary-to-primary isotopic ratio (^{29}Si/^{28}Si and ^{30}Si/^{28}Si) with decreasing Galactocentric radius (Wilson 1999). Furthermore, Monson et al. (2017) reported a higher ^{30}Si/^{29}Si in the ISM than both solar and pre-solar SiC grains. This indicates that the chemical evolution of the two secondary isotopes of Si within the Galaxy might have been different. This result can be explained if a mass-dependent isotopic fractionation were in

place, where the heavier isotopes evolve differently than the main isotope. We do not see this behaviour within L1157-B1, whose ^{29}SiO/^{30}SiO corresponds within error bars to the solar value throughout the whole source (see the lower panel in Fig. 3). If a mass-dependent isotopic fractionation occurs within our Galaxy, as suggested in Monson et al. (2017), it does not occur on the timescales probed with L1157-B1 (∼1000 yr), that is, within the time that the material that sputtered from the dust grains has to react in the gas phase and to evolve chemically.

5.2. Jet of L1157-mm

Jets are pivotal in the early stages of star-formation because they allow the accretion of mass from the disc onto the star by extracting angular momentum. While towards L1157 we see the effect of the jet impacting the gas (Tafalla & Bachiller 1995; Gueth et al. 1996; Benedettini et al. 2012), the only direct observational evidence of the jet associated with L1157-mm so far is spectra of the SiO bullets (Tafalla et al. 2015) and the maps of the high-velocity CO and SiO bullets (Podio et al. 2016), which were both detected close to the protostar. We present here for the first time a very high velocity bullet in SiO, showing the high-velocity jet at the position of the B0 shocked region working surface (at a distance of 68″, i.e. 0.12 pc, from the protostar). This SiO bullet is barely recognisable in the channel maps presented in Fig. 2 of Gueth et al. (1998) (lower panel to the right, at −18.3 km s^{-1}). Moreover, the velocity found in the high-velocity SiO bullet B0 is compatible with the velocity of the high-velocity bullets detected close to L1157-mm in Podio et al. (2016) when we take the precession pattern into account. A high-velocity feature has been observed in CS (see the red curve in Fig. 9 of Benedettini et al. 2013) towards the same position. The spectrum extracted from the peak of the high-velocity channel (blue solid line) in Fig. 5 shows the signature of the jet impacting the gas and creating the shocked region B0. A similar spectral feature has previously been observed towards L1448-B1 in Nisini et al. (2007), see their spectrum in the bottom left corner in Fig. 2, and towards IRAS 04166+2706 in Tafalla et al. (2010), see the top right spectrum in their Fig. 3.

5.3. B1a clump and its surrounding gas

The high spatial resolution of the new SOLIS SiO observations coupled with single-dish observations allow us to provide stringent constraints on the gas that is shocked at the B1a position and its surrounding gas. The analysis and the derived gas parameters are discussed in Sect. 4 and are summarised in Table 2.

The SiO-emitting gas in B1a, both the HV and EHV components, is heated to about 180 K and its density is about 6×10^5 cm^{-3}: the SiO column density associated with the HV is about five times higher than that in the EHV gas in B1a. Similarly, the gas surrounding B1a is much colder, at about 30–40 K, and more tenuous by about a factor 3. The SiO column density of this cooler gas is the same as that in B1a, which is slightly surprising as a coincidence. In the following, we try to better understand the meaning of these findings and the implications.

A few years ago, Lefloch et al. (2012) carried out an analysis of the CO emission towards L1157-B1 using single-dish observations that covered the J = 1–0 up to J = 16–15 lines. They found that the spectra could be decomposed into three velocity components, defined by the slope of the intensity versus the velocity of each line spectrum. Although the velocity decomposition is different from that we used here, which is purely based on three different velocity intervals, it is interesting to note that in Lefloch et al. (2012) a component was also found, designated g1, which they associated with the shocked gas. Its sizes (∼10″), density (a few 10^6 cm^{-3}), and temperature (∼200 K) are similar to that of our component associated with B1a. Therefore, our new SOLIS observations suggest that the component g1 in Lefloch et al. (2012) is very likely dominated by emission from the shocked gas at B1a; this supports the association with shocked gas claimed in Lefloch et al. (2012). Incidentally, this indicates that an accurate non-LTE analysis of single-dish data can provide fairly correct information even at scales much smaller than the telescope beams that were used.

In addition to the g1 component, in Lefloch et al. (2012) two other components were also found, called g2 and g3, which are associated with the walls of the B1 and B2 cavities, respectively. The parameters of component g2 are similar to those of the cold component of our HV and EHV fit: the size is about 20″ , compared with our 20–25″, the temperature is about 60 K, compared with our 30–40 K, and the density is higher than a few 10^5 cm^{-3} , compared with our $\sim2\times10^5$ cm^{-3}. This means that the g2 component is probably at least in part associated with the gas surrounding B1a that encompasses the whole B1 clump.

The association of our B1a and cold components with the g1 and g2 components of the CO analysis in Lefloch et al. (2012) allow us to estimate the abundance of SiO in them. Specifically, Lefloch et al. (2012) found that the CO column density is $\sim1\times10^{16}$ and $\sim1\times10^{17}$ cm^{-2} in g1 and g2, respectively: when we assume a CO abundance of 10^{-4} with respect to H_2, this corresponds to a SiO abundance of about 5 and 0.5 $\times10^{-7}$ in B1a and its surrounding, respectively. Although substantially increased with respect to the SiO in the quiescent gas of molecular clouds ($\sim10^{-12}$, Martin-Pintado et al. 1992), the silicon in the gas phase, released because of the sputtering and shattering of the grain mantles and refractory cores, is still just a small fraction of its elemental abundance ($\sim3.5\times10^{-5}$, Wilson & Rood 1994). The remaining Si is likely still in the dust grains because they are not expected to be completely destroyed by shocks. When we assume that atomic Si is efficiently converted into SiO as soon as it reaches the gas-phase (Neufeld & Dalgarno 1989; Herbst et al. 1989), our results reach a good agreement with the models of Caselli et al. (1997) for a shock with a velocity between 30 and 35 km s^{-1}.

We finally discuss the nature and origin of the cold gas surrounding B1a. Based on its properties (temperature, density, and SiO abundance), this gas can be material entrained by the B1a shock, be itself cooled gas from previous (older) shocks, or be both. The presence of multiple shocks in B1 that occurred within 1500 yr was reported by Podio et al. (2016) and was successfully used by Codella et al. (2017, 2020) to identify chemical formation routes of molecules more complex than SiO. The probability is therefore high that the cold component is cooled shocked gas. However, the HV map of the SiO J = 2–1 line (Fig. 6) suggests that a more extended and probably entrained gas also contributes to the emission.

6. Conclusions

We presented here the first isotopic ratio maps of SiO towards a shocked region. From these interferometric maps we can infer that the (2–1) transition of the main isotopologue is optically thick within the whole region imaged, also at high velocities (up to −20 km s^{-1}). The isotopic ratio map of the two rarer isotopologues, ^{29}SiO and ^{30}SiO, shows a uniform value consistent with the solar value of [^{29}Si/^{30}Si] = 1.5.

Coupling the high spatial resolution of the new SOLIS data with the large single-dish dataset, we were able to place stringent constraints on the physical properties of the gas in L1157-B1. Our observations can be reproduced by a more compact, denser, and warmer gas component ($n_{H2} = 6 \times 10^5$ cm^{-3}, $T = 180$ K and $X_{Si} = 5 \times 10^{-7}$), and by a more extended, colder, and less dense gas component ($n_{H2} = 2 \times 10^5$ cm^{-3}, $T = 40$ K and $X_{Si} = 0.5 \times 10^{-7}$).

Furthermore, the high spectral resolution and sensitivity of the SOLIS dataset allowed us to identify a high-velocity bullet of SiO that traces the impact of the jet that arises from the protostar L1157-mm on the B0 clump. This opens a new laboratory for future studies to further unveil the complex physical and chemical structure of this source.

Acknowledgements. We thank the anonymous referee for valuable comments and suggestions. This work is based on observations carried out under project number L15AA with the IRAM NOEMA Interferometer [30 m telescope]. IRAM is supported by INSU/CNRS (France), MPG (Germany) and IGN (Spain). We are very grateful to all the IRAM staff, whose dedication allowed us to carry out the SOLIS project. This work was supported by (i) the PRIN-INAF 2016 "The Cradle of Life - GENESIS-SKA (General Conditions in Early Planetary Systems for the rise of life with SKA)", (ii) the program PRIN-MIUR 2015 STARS in the CAOS - Simulation Tools for Astrochemical Reactivity and Spectroscopy in the Cyberinfrastructure for Astrochemical Organic Species (2015F59J3R, MIUR Ministero dell'Istruzione, dell'Universitá della Ricerca e della Scuola Normale Superiore), (iii) the European Research Council (ERC) under the European Union's Horizon 2020 research and innovation programme, for the Project "The Dawn of Organic Chemistry" (DOC), grant agreement No 741002, and (iv) the European Marie Skłodowska-Curie actions under the European Union's Horizon 2020 research and innovation programme, for the Project "Astro-Chemistry Origins" (ACO), Grant No 811312.

References

Anders, E., & Grevesse, N. 1989, Geochim. Cosmochim. Acta, 53, 197
Arce, H. G., Santiago-García, J., Jørgensen, J. K., Tafalla, M., & Bachiller, R. 2008, ApJ, 681, L21
Bachiller, R., & Pérez Gutiérrez, M. 1997, ApJ, 487, L93
Bachiller, R., Pérez Gutiérrez, M., Kumar, M. S. N., & Tafalla, M. 2001, A&A, 372, 899
Busquet, G., Lefloch, B., Benedettini, M., et al. 2014, A&A, 561, A120
Benedettini, M., Viti, S., Codella, C., et al. 2007, MNRAS, 381, 1127
Benedettini, M., Busquet, G., Lefloch, B., et al. 2012, A&A, 539, L3
Benedettini, M., Viti, S., Codella, C., et al. 2013, MNRAS, 436, 179
Caselli, P., & Ceccarelli, C. 2012, A&ARv, 20, 56
Caselli, P., Hartquist, T. W., & Havnes, O. 1997, A&A, 322, 296
Ceccarelli, C., Maret, S., Tielens, A. G. G. M., et al. 2003, A&A, 410, 587
Ceccarelli, C., Bacmann, A., Boogert, A., et al. 2010, A&A, 521, L22
Ceccarelli, C., Caselli, P., Fontani, F., et al. 2017, ApJ, 850, 176
Cheng, Y., Qiu, K., Zhang, Q., et al. 2019, ApJ, 877, 112
Codella, C., Benedettini, M., Beltrán, M. T., et al. 2009, A&A, 507, L25
Codella, C., Fontani, F., Ceccarelli, C., et al. 2015, MNRAS, 449, L11
Codella, C., Ceccarelli, C., Caselli, P., et al. 2017, A&A, 605, L3
Codella, C., Ceccarelli, C., Bianchi, E., et al. 2020, A&A, 635, A17
Dayou, F., & Balança, C. 2006, A&A, 459, 297
Dubernet, M.-L., Alexander, M. H., Ba, Y. A., et al. 2013, A&A, 553, A50
Fontani, F., Codella, C., Ceccarelli, C., et al. 2014, ApJ, 788, L43
Frank, A., Ray, T. P., Cabrit, S., et al. 2014, Protostars and Planets VI (Tucson: University of Arizona Press), 451
Gueth, F., Guilloteau, S., & Bachiller, R. 1996, A&A, 307, 891
Gueth, F., Guilloteau, S., & Bachiller, R. 1998, A&A, 333, 287
Guillet, V., Pineau Des Forêts, G., & Jones, A. P. 2011, A&A, 527, A123
Gusdorf, A., Cabrit, S., Flower, D. R., & Pineau Des Forêts, G. 2008a, A&A, 482, 809
Gusdorf, A., Pineau Des Forêts, G., Cabrit, S., & Flower, D. R. 2008b, A&A, 490, 695
Herbst, E., Millar, T. J., Wlodek, S., et al. 1989, A&A, 222, 205
Hoppe, P., Rubin, M., & Altwegg, K. 2018, Space Sci. Rev., 214, 106
Kong, S., Arce, H. G., Maureira, M. J., et al. 2019, ApJ, 874, 104
Lefloch, B., Cabrit, S., Busquet, G., et al. 2012, ApJ, 757, L25
Lefloch, B., Gusdorf, A., Codella, C., et al. 2015, A&A, 581, A4
Lefloch, B., Ceccarelli, C., Codella, C., et al. 2017, MNRAS, 469, L73
Lefloch, B., Bachiller, R., Ceccarelli, C., et al. 2018, MNRAS, 477, 4792
Mangum, J. G., & Shirley, Y. L. 2015, PASP, 127, 266
Martin-Pintado, J., Bachiller, R., & Fuente, A. 1992, A&A, 254, 315
Monson, N. N., Morris, M. R., & Young, E. D. 2017, ApJ, 839, 123
Müller, H. S. P., Spezzano, S., Bizzocchi, L., et al. 2013, J. Phys. Chem. A, 117, 13843
Neufeld, D. A., & Dalgarno, A. 1989, ApJ, 340, 869
Nisini, B., Codella, C., Giannini, T., et al. 2007, A&A, 462, 163
Ospina-Zamudio, J., Lefloch, B., Favre, C., et al. 2019, MNRAS, 490, 267
Podio, L., Codella, C., Gueth, F., et al. 2016, A&A, 593, L4
Podio, L., Codella, C., Lefloch, B., et al. 2017, MNRAS, 470, L16
Roelfsema, P. R., Helmich, F. P., Teyssier, D., et al. 2012, A&A, 537, A17
Schilke, P., Walmsley, C. M., Pineau des Forets, G., & Flower, D. R. 1997, A&A, 321, 293
Tafalla, M., & Bachiller, R. 1995, ApJ, 443, L37
Tafalla, M., Santiago-García, J., Hacar, A., & Bachiller, R. 2010, A&A, 522, A91
Tafalla, M., Bachiller, R., Lefloch, B., et al. 2015, A&A, 573, L2
Timmes, F. X., & Clayton, D. D. 1996, ApJ, 472, 723
Tychoniec, Ł., Hull, C. L. H., Kristensen, L. E., et al. 2019, A&A, 632, A101
Wilson, T. L. 1999, Rep. Prog. Phys., 62, 143
Wilson, T. L., & Rood, R. 1994, ARA&A, 32, 191
Zucker, C., Speagle, J. S., Schlafly, E. F., et al. 2019, ApJ, 879, 125

Appendix A: Channel maps

Figures A.1 and A.3 show the channel maps of the observed SiO isotopologues (see Table 1) with low-velocity resolution (7.3 km s^{-1}). Figures A.4 show the channel maps of the main isotopologue observed with high-velocity resolution (0.5 km s^{-1}).

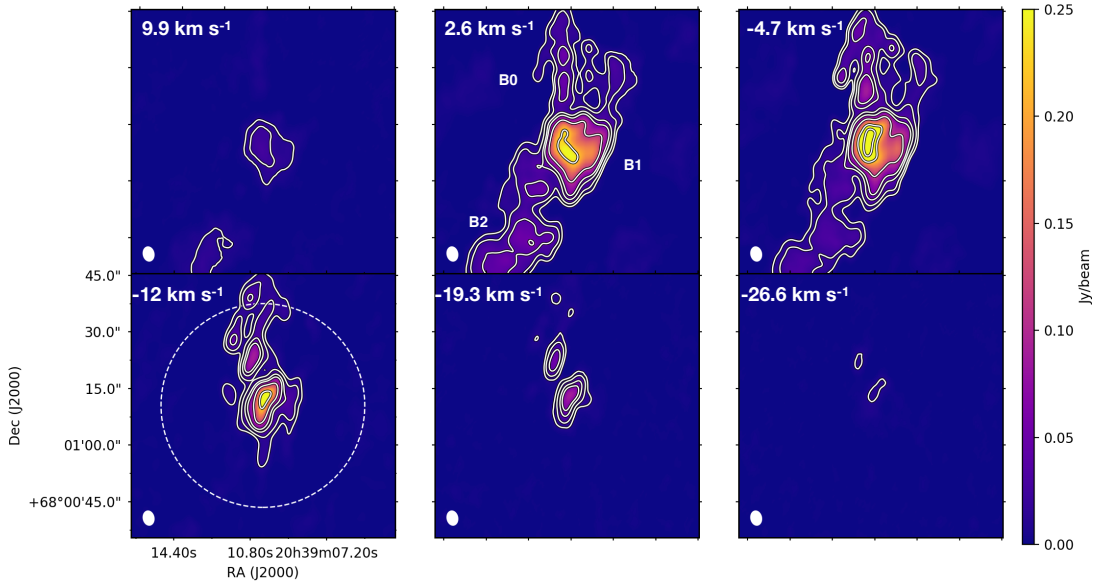

Fig. A.1. ^{28}SiO channel maps observed with a spectral resolution of 7.3 km s^{-1}. The clean beam of 3.8″ × 2.8″ is shown in the bottom left corner of the maps, and the primary beam of 56″ is reported as a dashed white circle in the *bottom left panel*. The contours are 10, 20, and 40, 60 and 120, and 250 and 350σ (rms = 0.9 mJy beam^{-1}) in the three panels.

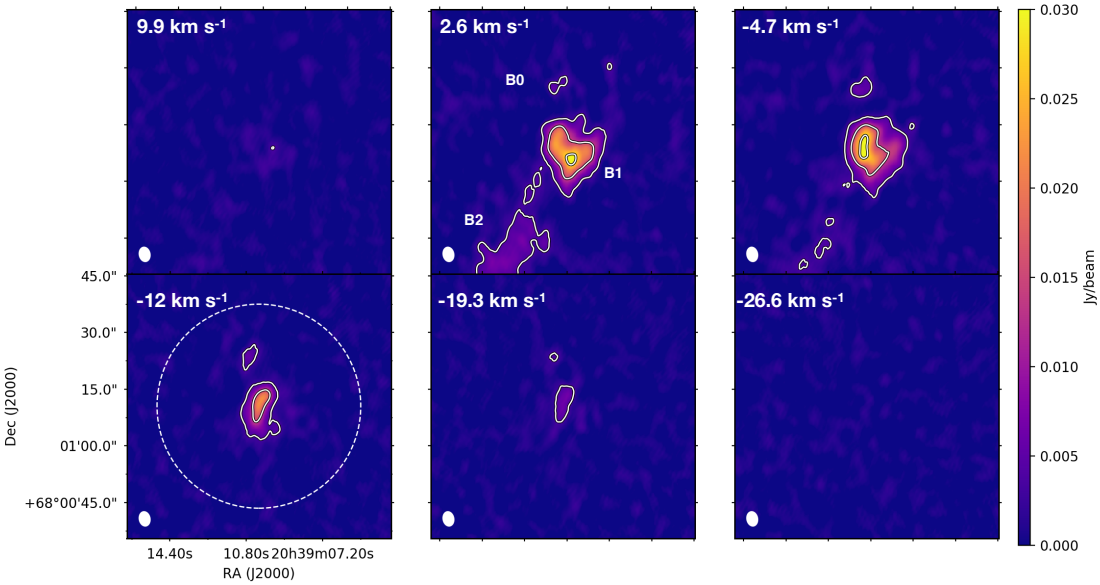

Fig. A.2. ^{29}SiO channel maps observed with a spectral resolution of 7.3 km s^{-1}. The clean beam of 3.8″ × 2.8″ is shown in the bottom left corner of the maps, and the primary beam of 56″ is reported as a dashed white circle in the *bottom left panel*. The contours are 5, 20, and 40σ (rms = 0.7 mJy beam^{-1}).

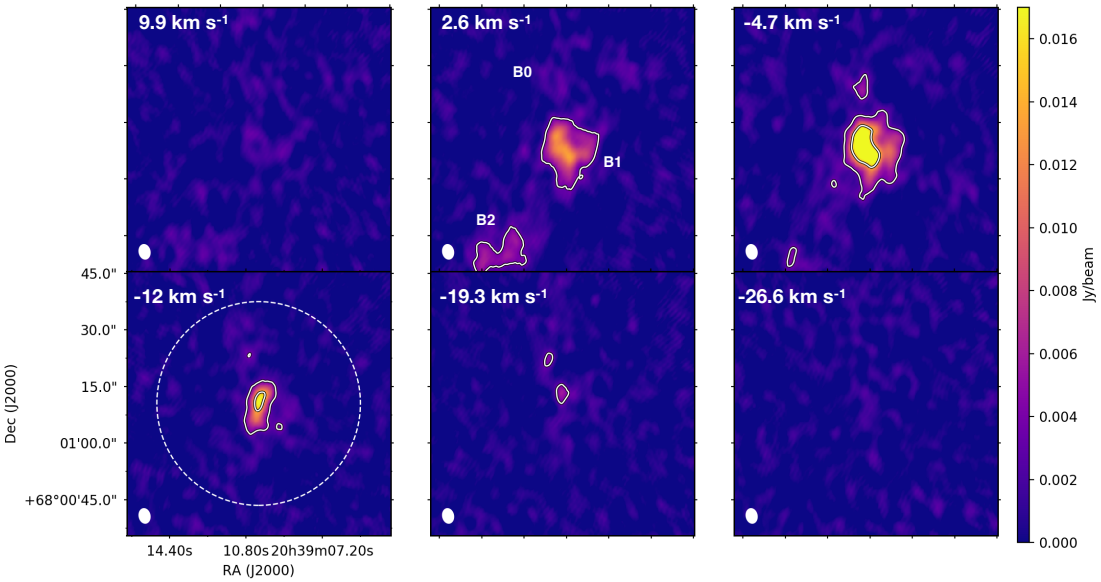

Fig. A.3. ^{30}SiO channel maps observed with a spectral resolution of 7.3 km s^{-1}. The clean beam of $3.8'' \times 2.8''$ is shown in the bottom left corner of the maps, and the primary beam of $56''$ is reported as a dashed white circle in the *bottom left panel*. The contours are 5 and 20σ (rms = 0.7 mJy beam^{-1}).

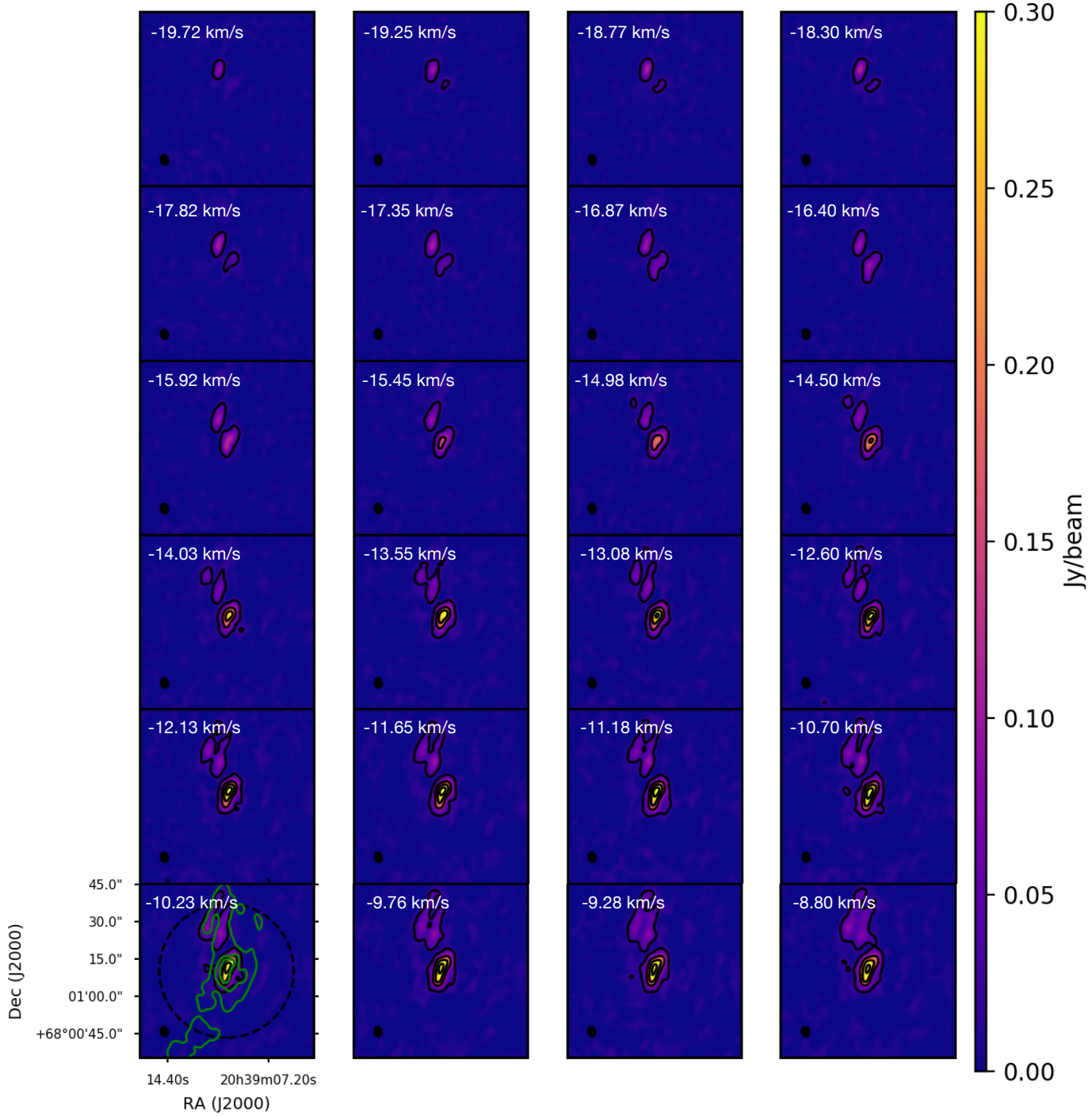

Fig. A.4. ^{28}SiO channel maps observed with a spectral resolution of ~0.5 km s^{-1}. The clean beam of 3.8″ × 2.8″ is shown in the bottom left corner of the maps, and the primary beam of 56″ is reported as a dashed black circle. The green contours in the channel maps show the 10, 60, and 120σ levels of the integrated intensity map of the ^{28}SiO, as shown in Fig. 1. The central velocity of the channel is reported in the top left corner of each panel.

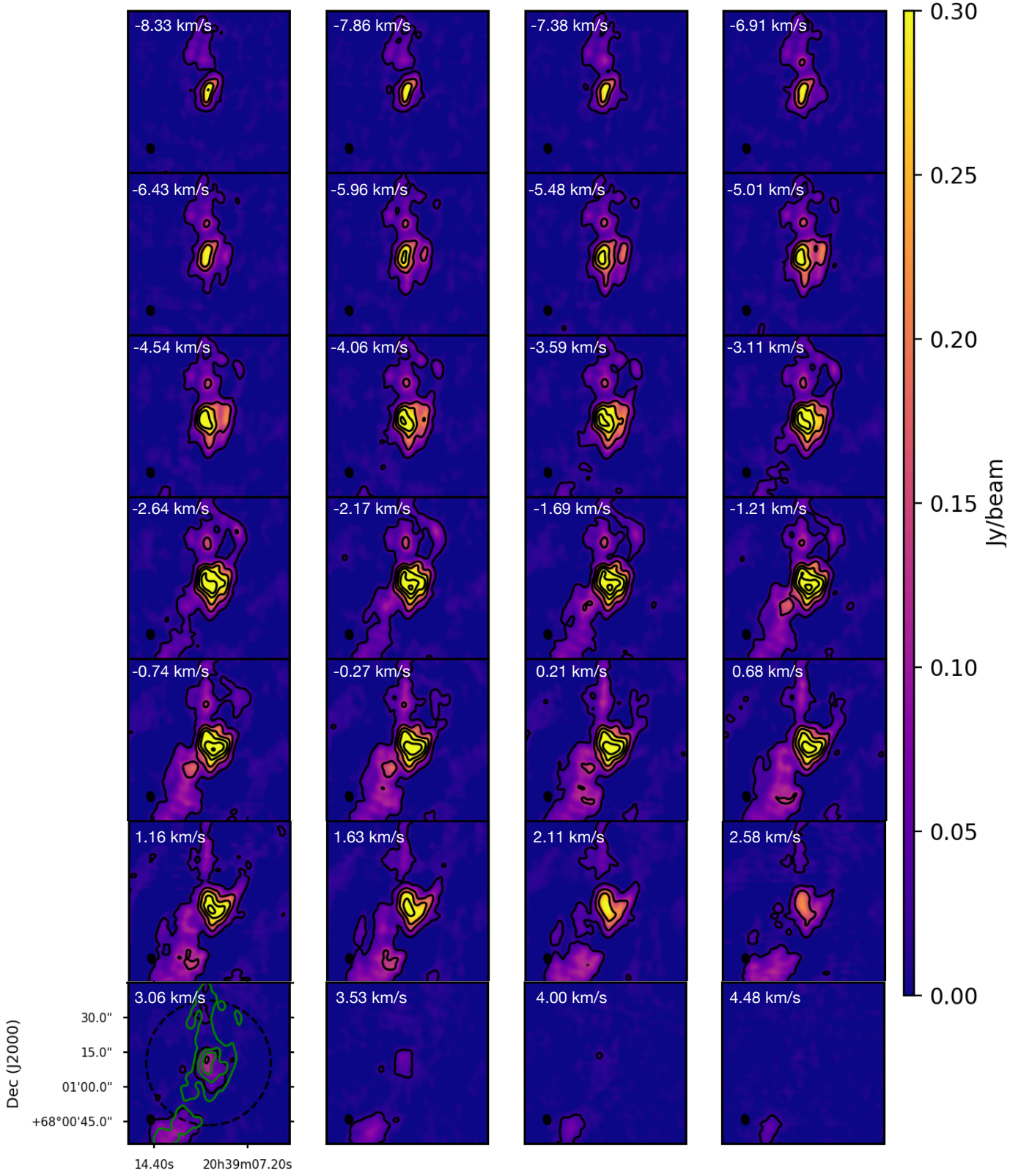

Fig. A.4. continued.

Appendix B: Missing flux

The spectra of the main isotopologue ^{28}SiO observed with NOEMA were compared with the spectrum observed with the IRAM 30 m antenna to evaluate the missing flux of the present NOEMA dataset. The comparison is shown in Fig. B.1. About 80% of the flux is recovered.

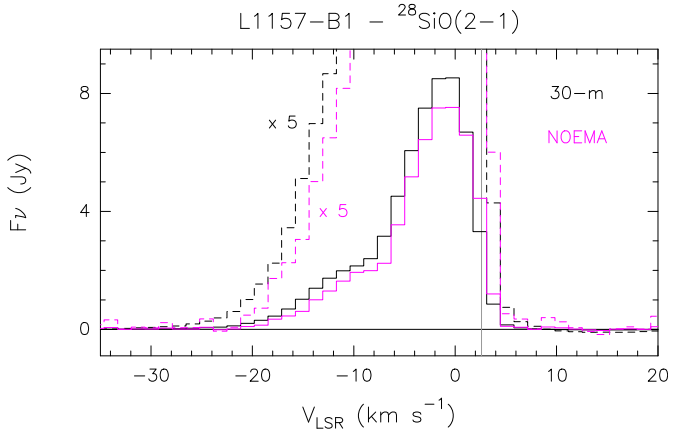

Fig. B.1. ^{28}SiO 2–1 intensity profile extracted from the data cube averaged within a 30″ beam (magenta line) over-plotted on the IRAM 30 m spectrum (*HPBW* ∼ 30″) (black histogram).